

Journal Pre-proofs

Vibrational spectroscopic, thermophysical, and structural properties of two Antarctic howardites: EET 87503 and QUE 97001

Ozan Unsalan, Cisem Altunayar-Unsalan, Bernardo A. Nogueira, Melanie Kaliwoda, Rui Fausto

PII: S0273-1177(25)00773-2
DOI: <https://doi.org/10.1016/j.asr.2025.07.038>
Reference: JASR 18583

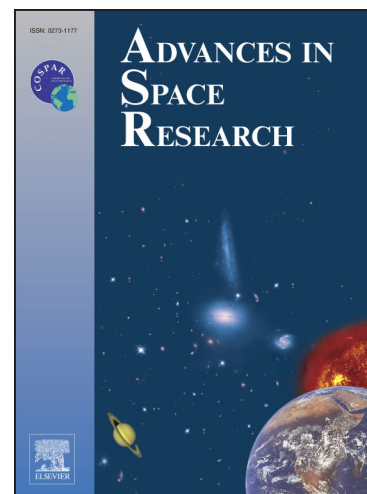
To appear in: *Advances in Space Research*

Received Date: 14 November 2024
Revised Date: 11 July 2025
Accepted Date: 14 July 2025

Please cite this article as: Unsalan, O., Altunayar-Unsalan, C., Nogueira, B.A., Kaliwoda, M., Fausto, R., Vibrational spectroscopic, thermophysical, and structural properties of two Antarctic howardites: EET 87503 and QUE 97001, *Advances in Space Research* (2025), doi: <https://doi.org/10.1016/j.asr.2025.07.038>

This is a PDF file of an article that has undergone enhancements after acceptance, such as the addition of a cover page and metadata, and formatting for readability, but it is not yet the definitive version of record. This version will undergo additional copyediting, typesetting and review before it is published in its final form, but we are providing this version to give early visibility of the article. Please note that, during the production process, errors may be discovered which could affect the content, and all legal disclaimers that apply to the journal pertain.

© 2025 COSPAR. Published by Elsevier B.V. All rights are reserved, including those for text and data mining, AI training, and similar technologies.



Vibrational spectroscopic, thermophysical, and structural properties of two Antarctic howardites: EET 87503 and QUE 97001

Ozan Unsalan,^{a,*} Cisem Altunayar-Unsalan,^b

Bernardo A. Nogueira,^{c,d} Melanie Kaliwoda,^e Rui Fausto^{c,f}

^aEge University, Faculty of Science, Department of Physics, 35100, Bornova, Izmir, Türkiye

^bEge University, Graduate School of Natural and Applied Sciences, 35100, Bornova, Izmir, Türkiye

^cCQC-IMS, University of Coimbra, Department of Chemistry, P-3004-535 Coimbra, Portugal

^dInternational Iberian Nanotechnology Laboratory (INL), P-4715-330 Braga, Portugal

^eMineralogical State Collection Munich (SNSB), D-80333 Munich, Germany

^fERA-Chair Spectroscopy@IKU, Istanbul Kultur University, Faculty Sciences and Letters, Department of Physics, 34158 Bakirkoy, Istanbul, Türkiye

Abstract

This study uses optical microscopy, Raman spectroscopy, differential scanning calorimetry (DSC), and thermogravimetric analysis (TGA) to examine the Antarctic howardite meteorites EET 87503 and QUE 97001. DSC results revealed troilite phase transitions in EET and QUE at 146.66 and 147.50 °C, corresponding to 0.26% and 0.13% troilite content, respectively. TGA indicated minor weight loss (< 1%) in both samples, with EET showing 0.399% and QUE 0.638% weight loss upon heating up to 1200 °C. Raman spectroscopy confirmed the presence of key minerals, including enstatite, ferrosilite, diopside, forsterite, ilmenite, and anorthite, as well as, in the case of the QUE 97001 meteorite, monticellite, a rare magnesium-end-member silicate olivine type mineral, providing insights into the complex thermal and impact histories of these howardites. The present findings appear as a contribution to a better understanding of the mineralogy and thermal evolution of this type of meteorites, linking them to potential parent bodies such as asteroid 4Vesta.

Keywords: EET 87503, QUE 97001, infrared and Raman spectroscopy, thermal analysis, howardite.

*Corresponding author

1. Introduction

Howardite class of meteorites is usually associated with 4Vesta, as they are thought to be excavated from Vesta surface (Righter, 2020). These achondrites are polymict breccias primarily composed of clasts and mineral fragments originating from eucritic and diogenitic sources (Duke and Silver, 1967; Wahl, 1952). According to the Meteoritical Bulletin (“Meteorit. Bull. Database,” 2025) as of 14th of October 2024, there are only 463 registered howardites (“List of howardites in Meteoritical Bulletin,” 2024) among all the 83,026 registered meteorites, i.e. this type of meteorites constitutes only ca. 5.6 per thousand (5.6‰) of the registered meteorites, which testifies its rarity. Among the whole HED (Howardite-Eucrite-Diogenite) clan (total 3037 samples), the fraction of howardite meteorites is about 0.15%. So far, only 155 howardites have been recovered from Antarctica (~33% of total howardites).

The two Antarctic howardites investigated in the present study are EET 87503 (EET) (collected at the Texas Bowl ice field in Antarctica) and QUE 97001 (QUE) (Queen Alexandra Range) (Fig. 1). EET and one of its pairings, EET 87513, were previously determined to have similar compositions regarding percentage (in the 69-72% range) of percentage of eucritic material (POEM), which is consistent with well-blended regolithic howardites (Mittlefehldt et al., 2013). Previous reports on EET (Hodges and Mittlefehldt, 2017; Mittlefehldt et al., 2013) suggested that this howardite is a regolith breccia dominated by debris from the parent asteroid, with a small component of admixed chondritic impactor debris. EET was previously analyzed in terms of its K, Ti, Th abundance (Tian, 2021). QUE was less intensively studied. By using ($^{40}\text{Ar}/^{39}\text{Ar}$) dating analysis, impact-melt clasts in QUE were investigated in order to obtain information on the Vestan cataclysm (Cohen, 2013). This meteorite was also among the five howardites (ALH 090004, EET 96002, MIL 07664, MIL 07664, and QUE 97001) used in an investigation which confirmed/supported the complexity of the current day Vestan surface (Cohen, 2013), based on the analysis of thin sections obtained from the five studied howardites, which revealed multiple eucrite composition clasts with different crystallization and thermal histories (Mayne et al., 2016). Besides, the near infrared spectrum of QUE was recorded for a spectroscopic comparison of HED meteorites and V-type asteroids in the inner Main Belt (Moskovitz et al., 2010).

Although campaigns to Antarctica require collection efforts and budget, it is crucial to find and recover such less-weathered specimens there in order to further elucidate and characterize these precious specimens and make connections to their potential parent asteroid/body. Given that the mineral and lithic clasts in these breccias may represent various portions of the differentiated crusts and have not been significantly altered by impact processes, these achondrites serve as a unique

source of information on the formation of the planet's early crust (Miyamoto et al., 1978). The present study is a collaborative investigation on the two selected howardites, combining results of optical microscopy, Raman spectroscopy, differential scanning calorimetric (DSC) and thermogravimetric analyses (TGA), aiming at contributing to a better understanding of the mineralogy and thermal evolution of this type of meteorite.



Fig. 1. EET 87503 (*left*) and QUE 97001 (*right*) howardite samples (bulk sample and thin section). The samples were obtained from the NASA Johnson Space Center Antarctic Meteorite Collection.

2. Experimental

2.1. Optical microscopy

The optical morphology of thin sections of EET and QUE was examined using a Leica 80M stereo microscope equipped with a Leica EC3 digital color camera. Transmitted light microscopy was employed, and the Leica EC3 camera offers high-resolution imaging with a 3.1-megapixel sensor.

2.2. Differential scanning calorimetry (DSC)

Samples were prepared according to the procedure reported by our group previously (Altunayar-Unsalan et al., 2025, 2021). Approximately ~10 mg of the howardite samples were ground in an agate mortar and the samples were encapsulated in standard aluminum hermetic DSC pans. An empty pan was used as a reference. The data were collected in a heat flux type TA Q20 DSC calorimeter (TA

Instruments Inc.), using a heating rate of $5\text{ }^{\circ}\text{C min}^{-1}$, within the range of temperature $-50\text{--}550\text{ }^{\circ}\text{C}$ ($223\text{--}823\text{ K}$), for troilite (FeS) determination. Temperature and heat flow calibrations of the instrument were done using indium (melting temperature: $156.6\text{ }^{\circ}\text{C}$) and 22.5 mg synthetic sapphire standard, respectively. The phase-transition enthalpy changes (ΔH) were determined by measuring the area under the phase transition peaks. Data analysis was performed with the Universal V4.5A TA Instruments software.

2.3. Thermogravimetric analysis (TGA)

The samples to be subjected to TGA measurement were prepared according to the procedure as we reported previously (Altunayar-Unsalan et al., 2021; Altunayar-Unsalan and Unsalan, 2022). Approximately $\sim 20\text{ mg}$ of ground sample of each meteorite was used for the determination of mass loss upon heating. The sample was placed in a ceramic cup ($90\text{ }\mu\text{L}$) and an empty ceramic cup was used as a reference. The measurements were carried out in an SDT Q600 apparatus (TA Instruments Inc., New Castle, Delaware, USA) instrument using a heating rate of $10\text{ }^{\circ}\text{C min}^{-1}$, in a temperature range between ambient ($\sim 25\text{ }^{\circ}\text{C}$ (298 K)) and $1200\text{ }^{\circ}\text{C}$ (1473 K), and a nitrogen (N_2) flow of 100 mL min^{-1} . The collected TGA data were analyzed using the Universal V4.5A TA Instruments software.

2.4. Raman spectroscopy

Raman measurements were performed at room temperature in a Horiba LabRam HR Evolution micro-Raman confocal system with a $50\times$ magnification objective lens (numerical aperture 0.55). Excitation was performed at 532.0 , 623.8 , or 785.0 nm , with the laser power at the sample kept within the $2\text{--}5\text{ mW}$ range, the spot size being $\sim 1\text{ }\mu\text{m}$. The used spectral resolution was 1.5 cm^{-1} in all cases, and the final spectra were built by averaging 5 to 20 individual spectra, which were collected with an acquisition time of $5\text{--}20\text{ s}$. No post processing was applied to the data, except for linear baseline correction. The Raman mapping measurements were performed in the same instrument, with laser excitation at 532.0 nm and a laser power at the sample of ca. 5 mW . The Raman maps were obtained in 2×2 and $1 \times 1\text{ mm}^2$ areas for QUE and EET samples, respectively, with a step size of $15\text{ }\mu\text{m}$, and autofocus (auto z -adjustment).

3. Results and discussion

3.1. Optical microscopy

The petrographic image of EET under transmitted light is given in Fig. 2. In this figure, the matrix predominantly consists of a light-colored mineral, which appears to be a brecciated texture typical of howardites and is related to the history of impact events. The most noticeable features are the small, rounded inclusions within the lighter minerals, identified as chrome-bearing spinels. These spinels are characterized by their darker brownish to reddish color, contrasting against the lighter matrix. The fractures and grain boundaries within the matrix are apparent, indicating a complex history of mechanical stress and recrystallization. These fractures often cut across the grains and are not confined to grain boundaries, suggesting they formed after the initial consolidation of the meteorite. The grains themselves vary in size, with some showing evidence of angular shapes indicative of fragmented clasts, which is consistent with the brecciated nature of howardites. The presence of spinels within the matrix may provide insights into the thermal and shock history of the meteorite, as these minerals are typically stable at high temperatures and pressures. Overall, the image captures the intricate and multifaceted nature of the meteorite's microstructure, reflecting its dynamic geological history.



Fig. 2. Chromite-bearing spinels in EET (transmitted light thin section photomicrograph).

In Fig. 3, (plane-polarized light), the prominent brownish clast is identified as clinopyroxene (cpx), exhibiting characteristic cleavage and fracture patterns indicative of its crystalline structure. Above the cpx clast, a whitish-grey clast appears, and this clast represents olivine (ol). The large

whitish grain at the bottom left was assigned as plagioclase (pl). This plagioclase was identified based on its optical properties under plane-polarized light, including its low relief, lack of pleochroism, and typical blocky morphology. As shown in Fig. 3, this plagioclase grain appears with low relief and a light gray-white appearance under plane-polarized light. It is non-pleochroic and displays the characteristic blocky to lath-shaped habit consistent with plagioclase in volcanic or subvolcanic rocks. This plagioclase grain appears relatively intact, with clear, well-defined boundaries, suggesting it may have been more resistant to shock metamorphism compared to the surrounding matrix. The large olivine crystal appears more resistant to shock metamorphism compared to the surrounding matrix, as evidenced by its relatively coherent internal structure and lack of fracturing. As seen in Fig. 4, the olivine crystal displays sharp birefringent colors, consistent extinction behavior, and a lack of planar deformation features, suggesting that it has preserved much of its original crystalline structure. In contrast, the surrounding matrix appears optically more heterogeneous, with localized darkening, finer-grained material, and potential isotropic patches, which are indicative of shock-related deformation and recrystallization or even partial glass formation. By "resistant," we refer to the relative preservation of olivine's crystal lattice, as it lacks the signs of high strain (e.g., mosaicism, planar fractures, or shock-induced recrystallization) observed elsewhere in the matrix. The overall image composition, featuring the clinopyroxene, plagioclase, and unidentified grey clast, encapsulates the heterogeneity of this howardite. This heterogeneity is a result of their formation through the aggregation of various rock fragments, each with its own thermal and impact history.

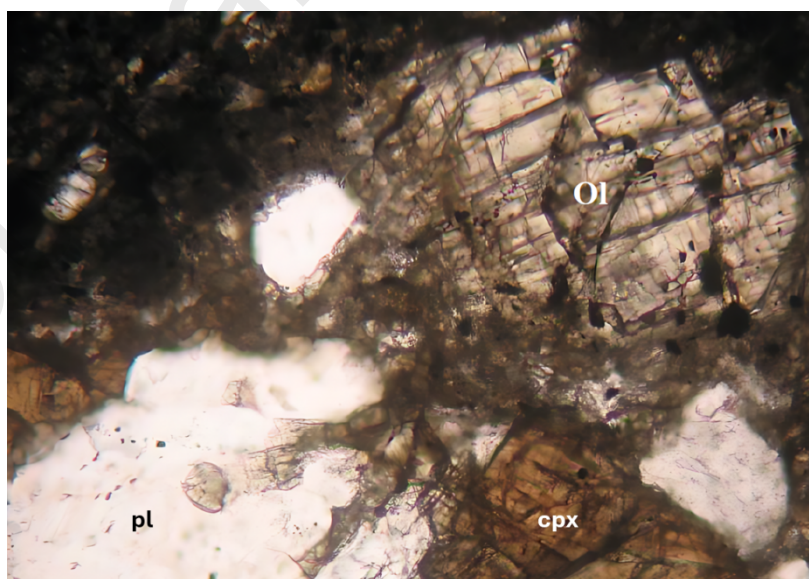


Fig. 3. Olivine and pyroxene in EET (plane-polarized thin section photomicrograph).

Fig. 4 demonstrates that the olivine crystal is crisscrossed by a network of fractures, which are irregular and vary in width. The fractures extend through the crystal, showing that they formed after the olivine had already crystallized. The presence of multiple intersecting fractures suggests a complex history of repeated stress events. Within the fractures, there are veins filled with secondary minerals that appear darker compared to the host olivine. These veins are formed from materials that infiltrated the fractures post-impact, suggesting fluid movement within the meteorite. The contrast between the bright olivine and the darker veins highlights the secondary alteration processes. Surrounding the olivine crystal, the matrix contains numerous rounded fragments and clasts of various colors and sizes. The matrix surrounding the olivine crystal consists of a fine-grained groundmass with embedded rounded fragments. The olivine crystal in this image shows clear signs of fracturing. Moreover, the fractures are visible as dark lines crisscrossing the bright yellow-green olivine crystal. These fractures are indicative of a mechanical stress, which could be due to shock metamorphism. The presence of these fractures in the olivine crystal is a typical feature observed in meteorites that have experienced significant impact events, leading to the internal breakage of the crystal structure.

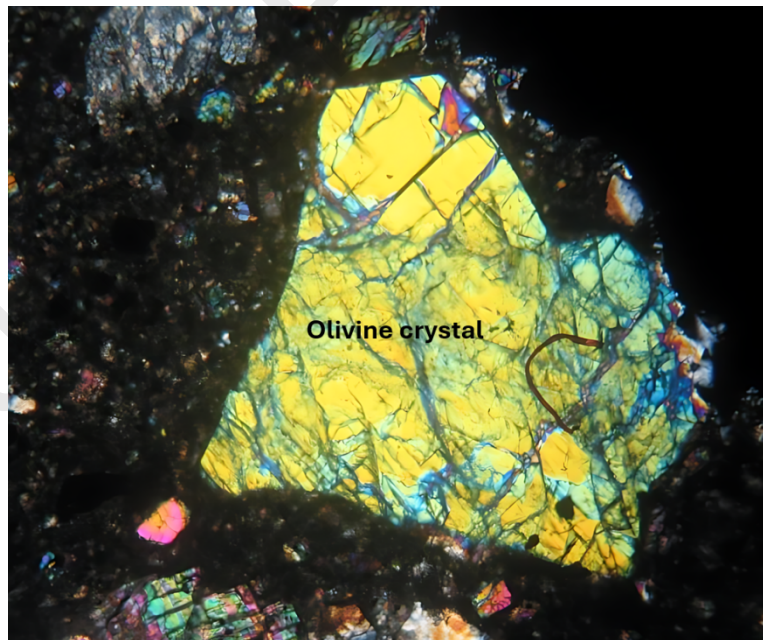


Fig. 4. Olivine crystal in QUE (cross-polarized thin section photomicrograph).

A cross-polarized thin section photomicrograph of QUE is shown in Fig. 5. At the center of the image, the prominent olivine grain displays a greenish hue under polarized light, exhibiting well-defined crystal boundaries and internal fractures. This olivine grain is surrounded by a large orthopyroxene grain, which dominates the middle portion of this section image. The orthopyroxene appears in varying shades of brown, indicating different orientations and possibly varying compositions within the grain. At the bottom middle and right, two smaller plagioclase grains, separated by the matrix, can be identified by their distinctive grey color. Surrounding these major mineral components, the finer-grained matrix consists of a mixture of other silicate minerals, contributing to the overall brecciated texture of the meteorite. In addition, Fig. 5 also shows fractured grains. The large, light-colored grain near the center of the image exhibits distinct fractures running through it. Furthermore, the colorful grains surrounding the central fractured opx grain also show signs of stress, with some displaying undulatory extinction, which is another indicator of shock metamorphism. The overall appearance of this section illuminated under cross-polarized light suggests that it has undergone significant impact-related deformation.

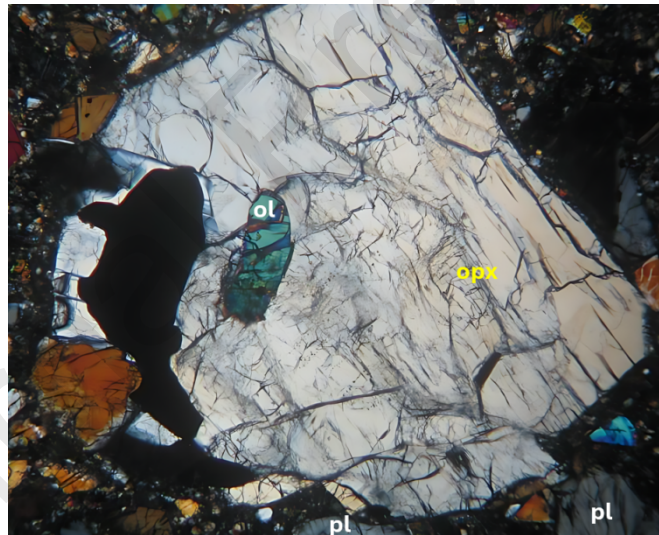


Fig. 5. Orthopyroxene, olivine and plagioclase in QUE (cross-polarized thin section photomicrograph).

Multiple optical microscopy features observed in the thin sections of EET and QUE indicate the presence of moderate shock metamorphism. For instance, in Fig. 5, plagioclase grains exhibit undulatory extinction and internal fracturing, while the orthopyroxene grain shows planar fractures. These are well-established indicators of shock stage S3 to S4, as defined by the optical shock classification (Stöffler et al., 1991) and further refined in subsequent studies (Jaret et al., 2014). Undulatory extinction in plagioclase and pyroxene is a result of dislocation movement under high

differential stress (>15 GPa), while the presence of planar fractures and deformation twins corresponds to pressure regimes typically between 15–35 GPa. In the QUE sample, the lack of complete maskelynitization of plagioclase, combined with these moderate deformation features, supports an assignment to intermediate shock stages. The heterogeneous appearance of the matrix, presence of isotropic zones, and angular brecciated clasts further support a history of repeated impact processing under moderate pressure and temperature conditions. These features are consistent with impact processing near the surface regolith of a differentiated parent body such as 4 Vesta.

3.2. Differential scanning calorimetry (DSC)

Fig. 6 presents the DSC curves highlighting the α/β phase transition of troilite, the iron-rich endmember of the pyrrhotite group of minerals, during the heating of the two studied howardites. These curves revealed that the troilite (FeS) existing in QUE and EET exhibits characteristic α/β phase transition at $T_{\alpha} = 147.50$ and 146.66 °C, respectively, corresponding to sharp endothermic DSC peaks. In our earlier work on another howardite (Sarıçiçek) we reported this transition of troilite at 148.98 °C [16], so that the present results are in line with those previous results. Allton *et al.* have also reported the α/β phase troilite transition between 142 and 150 °C for various L3, L7, octahedrite meteorites, and terrestrial troilite (EET 83212, PAT91501, Mundrabilla, and Del Norte, respectively) (Allton *et al.*, 1994).

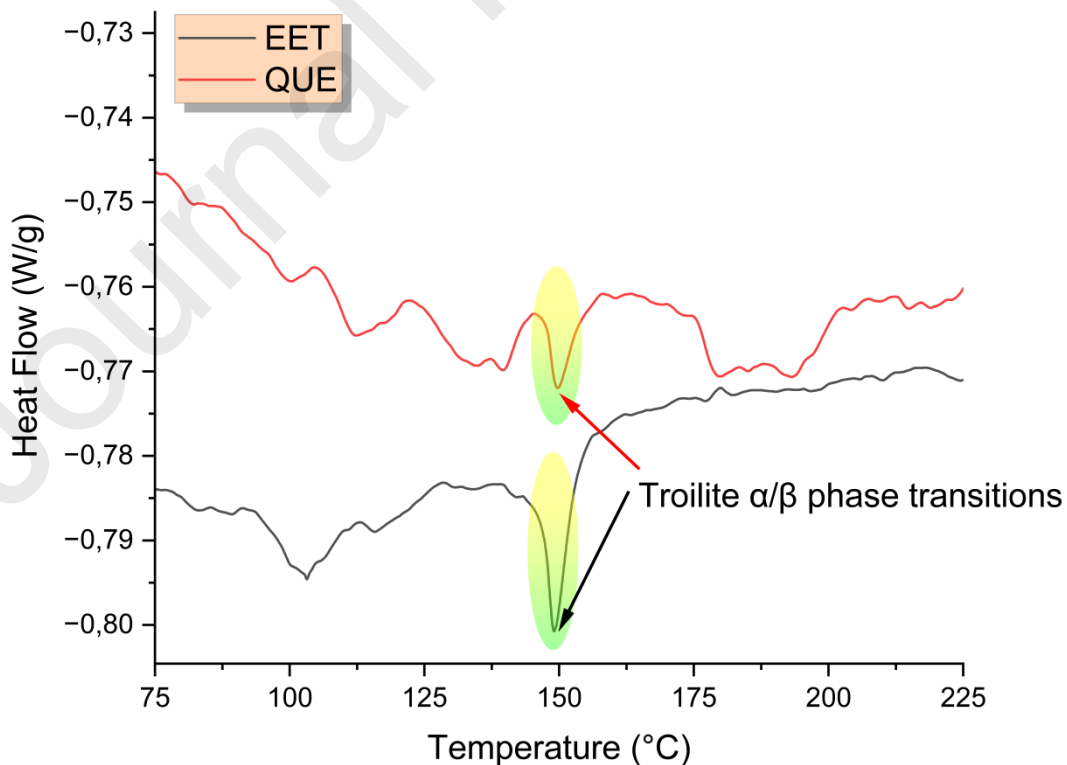


Fig. 6. DSC curves highlighting the α/β phase transition of troilite in EET and QUE.

Table 1 shows the observed onset temperature for the α/β phase transition (T_α), as well as the full-width-at-half-maximum ($\Delta T_{1/2}$) of the peak, and the enthalpy change (ΔH) for both howardites. The troilite content in QUE and EET were estimated by considering the corresponding measured α/β phase transition temperature and enthalpy change. For this, the obtained values of the enthalpy changes were divided by 42.5 J g^{-1} , which was established for pure troilite (Alton et al., 1994; Szurgot Wach, Radoslaw A., Przylibski, T., 2012), as suggested by Allton *et al.* (1994) (Allton et al., 1994) and also by Szurgot *et al.* (2012) (Szurgot Wach, Radoslaw A., Przylibski, T., 2012). The determined troilite contents by following this approach are 0.26 and 0.13 wt.% for EET and QUE, respectively, indicating that QUE has less troilite than EET. The troilite contents obtained for the studied meteorites do not differ considerably from those reported in previous studies on howardites (Maksimova et al., 2020, 2019; Unsalan et al., 2019) (e.g., 0.6 wt.% for Sariçiçek howardite, as determined from Mössbauer and XRD data). Previous results for a different EET subsample (EET 87503,10) reported by Jarosewich indicated a troilite content of 0.35 wt.%, which also agrees well with our results for EET 87503,204. Jarosewich has also analyzed other 4 howardites and found their troilite contents to be 0.77, 0.55, 0.96, and 0.74 wt.% for Bholgati, Bialystok, Bununu, and Petersburg howardites, respectively (with average wt.% of 0.76), which are also in good agreement with the present results.

Table 1. T_α , full-width-at-half-maximum ($\Delta T_{1/2}$), and enthalpy change ($\Delta H_{\alpha/\beta}$) of the DSC peak associated with the α/β phase transition of troilite in EET and QUE.

Sample	T_α		
	T_{onset} (°C)	$\Delta T_{1/2}$ (°C)	$\Delta H_{\alpha/\beta}$ (J g ⁻¹)
EET	146.66	3.82	0.1095
QUE	147.50	4.06	0.0543

3.3. Thermogravimetric analysis (TGA)

TGA was used to determine the weight loss undergone by the howardite samples upon heating from ambient temperature to 1200 °C. The decrease in weight is connected with the loss of volatile components, in particular of hydroxides and phyllosilicates, which are markers of water-induced modification (Nakashima et al., 2013). Fig. 7 depicts the TGA findings for the two howardite fragments. As shown in the figure, for EET and QUE the obtained total weight-loss was found to be small, amounting to only 0.39 and 0.64%, respectively.

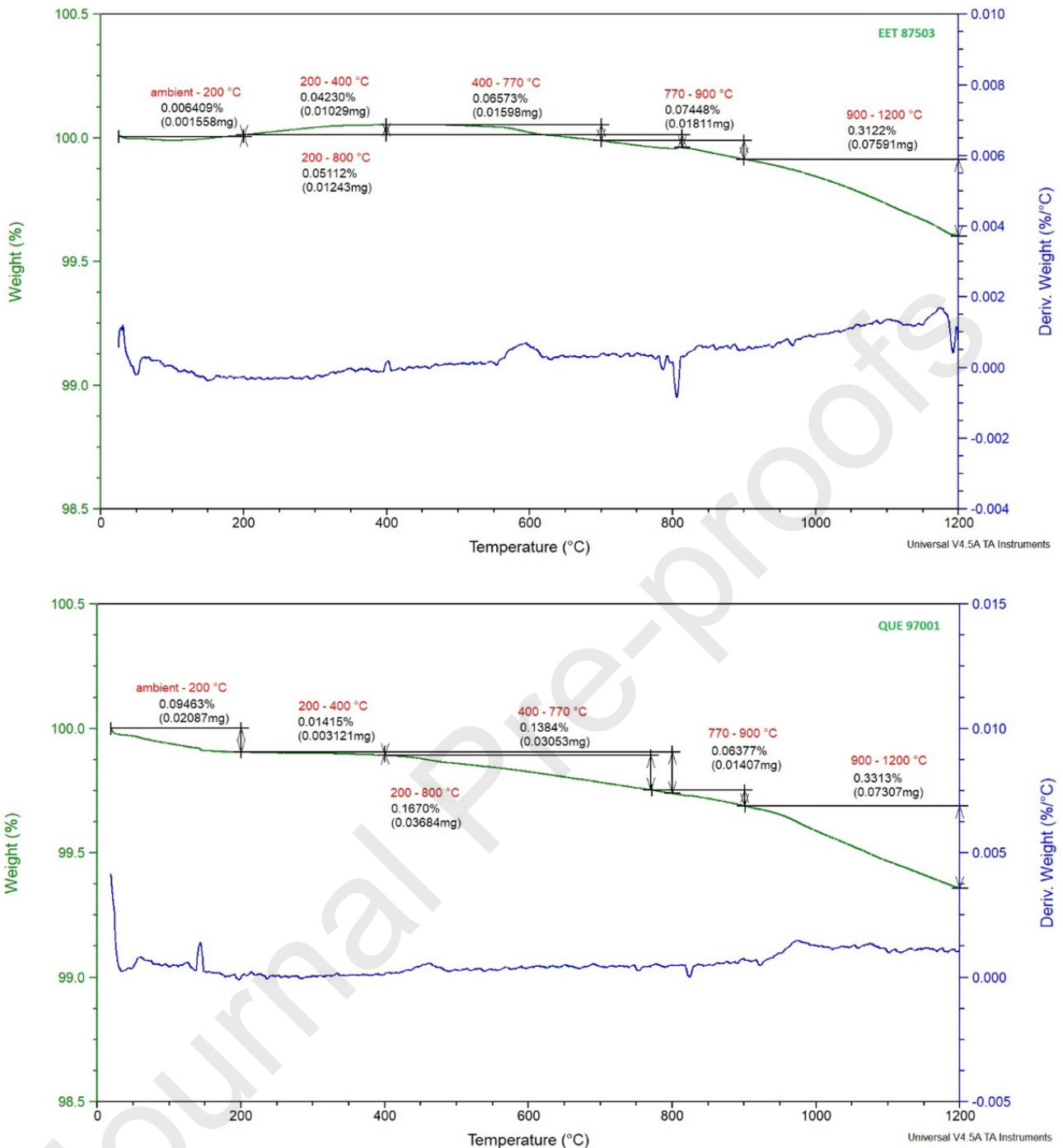


Fig. 7. TGA curves for EET (*top*) and QUE (*bottom*).

The first derivative of the TGA curves (derivative thermogravimetric function, DTG, shown in blue color in Fig. 7) may be used for identification of the host mineral containing the volatile components being released along the performed heating (Garenne et al., 2014; Potin et al., 2020). According to Garenne *et al.* (Garenne et al., 2014), TGA and DTG profiles may be divided into four different temperature ranges to evaluate compositional parameters of meteorites : (i) the first range (between room temperature and 200 °C) is associated with the release of molecular water, which

gives rise to two peaks in this temperature range, the first, at ~ 80 °C, caused by the release of adsorbed water molecules, and the second, over 100 °C, attributed to the release of mesopore water; (ii) the second range (200-400 °C) is informative for the release of water from (oxy)-hydroxide minerals, such as the decomposition of ferrihydrite and goethite at around 240 °C; (iii) the third range (400-770 °C) corresponds to release of hydroxyl groups from phyllosilicates and the decomposition of iron sulfates, like troilite, pyrite, and pyrrhotite; and, finally, the (iv) range, between 770 and 900 °C, which is associated with the release of CO₂ from carbonates and SO₂ from sulfates.

Since in the studied samples no water release was detected below 200 °C, it can be concluded that the samples have not been significantly weathered. In addition, despite the difficulty to precisely determine the exact type of minerals by TGA, we do not rule out the decomposition of terrestrial carbonates which show very low weight losses of <1%, as previously reported (Garenne et al., 2014; King et al., 2015) for several carbonaceous chondrites, rather than howardites.

In Fig. 7, TGA curve for EET sample showed an increase in weight above 100%. This indicates some type of external effect that might be an absorption of moisture or gas due to the open crucibles used. Thus, the sample may be interacting with the atmosphere (e.g., absorbing water vapor, carbon dioxide, or oxygen), causing this apparent weight gain. This effect was not observed for QUE. Another possible reason for this could be oxidation reactions, where the sample undergoes oxidation during heating, the formation of oxides could cause an increase in mass. Regarding the positive and negative peaks observed in DTG curves for both samples, the positive peaks in curves correspond to the rate of mass loss. A positive peak indicates a phase of the experiment where the sample is rapidly losing mass due to decomposition, evaporation, or some other reaction (e.g., volatilization or decomposition of organic components). In addition, negative ones in the DTG curves are less common but can occur. These might represent periods where the sample mass appears to increase, often corresponding to phenomena like reabsorption of gases or moisture leading to an apparent mass gain. Also, endothermic processes such as phase transitions that change the mass signal cause these mass signals to go down.

3.4. Raman spectroscopy

Raman spectra of different parts of the meteorites' samples appearing distinct at the optical microscope were collected in order to determine the nature of the major mineral constituents of each sample. Raman maps were then produced for selected regions of the samples, to evaluate the distribution of the minerals in these regions.

3.4.1. QUE sample

In QUE sample, the following minerals were identified by Raman spectroscopy: (1) an orthopyroxene with high content of enstatite (MgSiO_3), (2) diopside (clinopyroxene, $\text{MgCaSi}_2\text{O}_6$), (3) anorthite (plagioclase feldspar, $\text{CaAl}_2\text{Si}_2\text{O}_8$), (4) ilmenite (FeTiO_3), and (5) monticellite (olivine, CaMgSiO_4) (Figs. 8 and 9).

The Raman spectrum of the orthopyroxene in QUE is shown in Fig. 8a. This spectrum can be compared with the reference spectrum of enstatite (Lafuente et al., 2015) shown in Fig. 8b (the two spectra are also plotted together in Fig. 8c for better comparison). According to Huang et al (Huang et al., 2000) the frequencies of the bands observed in the Raman spectra of orthopyroxenes can be used to estimate the enstatite:ferrosilite wt% ratio. The frequencies of the most prominent bands observed in the orthopyroxene present in the QUE meteorite, assigned to the symmetric stretching vibrations of the non-bridging Si–O (1006 cm^{-1}) and Si–O–Si bridging (659 and 679 cm^{-1}) moieties, and to Mg/Fe–O stretching (338 cm^{-1}) vibrations (Huang et al., 2000; Kakkala, 1993), led to the conclusion that the orthopyroxene found in the meteorite has a composition corresponding roughly to the enstatite:ferrosilite 80:20 wt% ratio ($\text{En}_{80}\text{Fs}_{20}$) (Huang et al., 2000).

According to the Raman data shown in Fig. 8d-f, the clinopyroxene material present in the QUE sample is diopside ($\text{MgCaSi}_2\text{O}_6$), the magnesium endmember of the diopside–hedenbergite series. Indeed, although diopside forms a complete solid solution series with hedenbergite ($\text{FeCaSi}_2\text{O}_6$), the Raman spectrum of the examined meteoritic clinopyroxene shows a very good match with that of diopside, which is far better than with those of other possible candidates (e.g., clinoenstatine, hedenbergite). The Raman spectrum of diopside has been extensively studied both experimentally and theoretically (Downs, 2006; Etchepare, 1972; Kakkala, 1993; Prencipe et al., 2012), and the effect of crystal orientation on the spectral profile obtained upon excitation with polarized light were evaluated (Prencipe et al., 2012). The characteristic most intense band marks for this mineral are observed in the spectrum of the clinopyroxene QUE at 328 , 393 , 667 and 1011 cm^{-1} , which compare well with the data reported by Prencipe *et al.* (Prencipe et al., 2012) (323 , 389 , 667 and 1013 cm^{-1}). Based on a series of detailed full-periodic quantum chemical calculations of the Raman spectrum of diopside (Prencipe et al., 2012), the bands observed in the 300 - 400 cm^{-1} range have been ascribed to bending (tilting) vibrations of the Si–O tetrahedral structures in the diopside crystal, the band observed at 667 cm^{-1} to the Si–O–Si bridges symmetric stretching mode, and the one observed at 1013 cm^{-1} to the symmetric stretching vibrations of the non-bridging Si–O moieties (Prencipe et al., 2012).

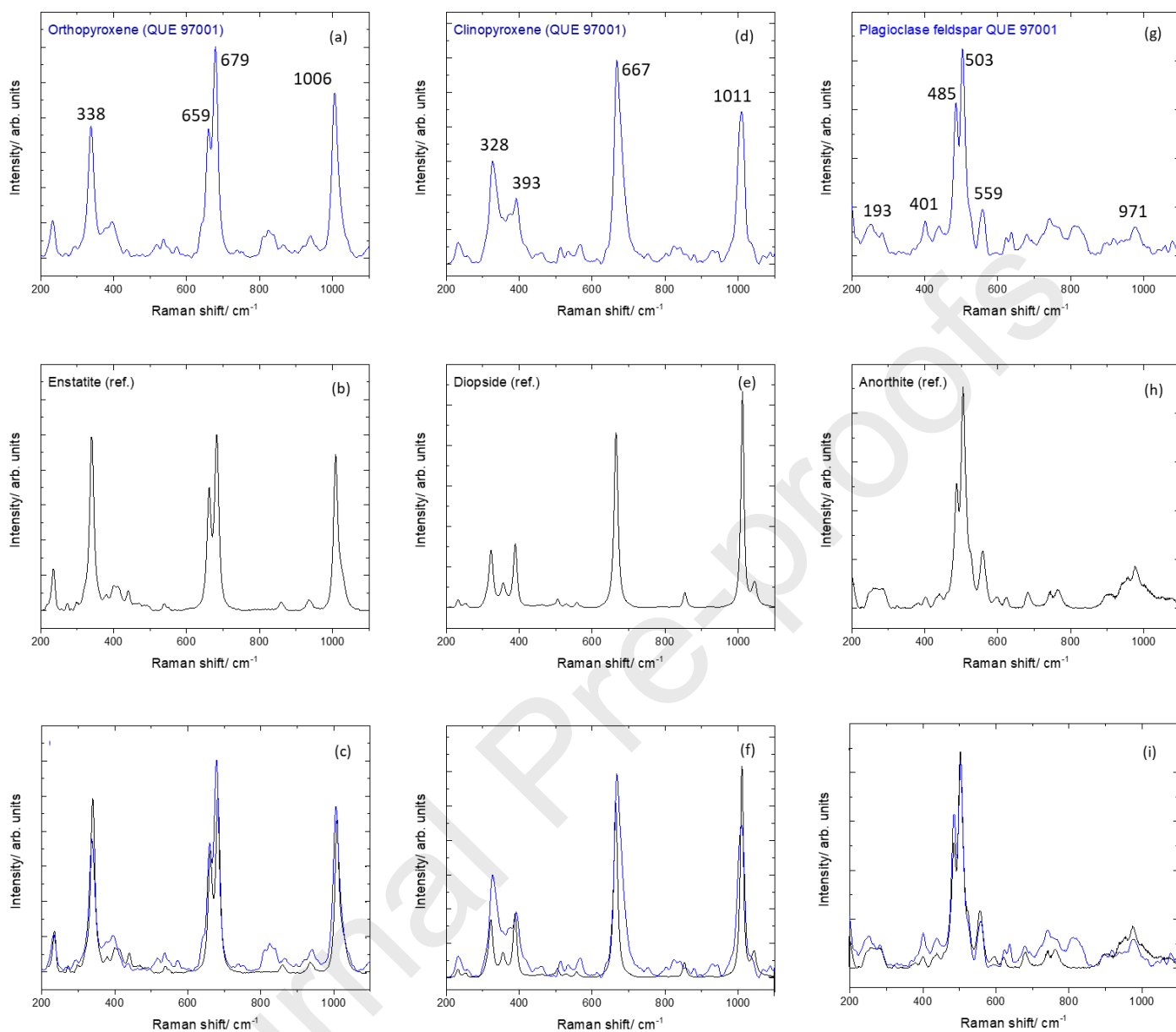


Fig. 8. Raman spectra of the (a) orthopyroxene-, (d) clinopyroxene-, and (g) plagioclase feldspar-type materials obtained from the QUE meteorite sample, and the spectra of the reference minerals, (b) enstatite, (e) diopside, and (h) anorthite. The spectra of the observed minerals and of the corresponding references are also plotted together in graphs (c), (f) and (i). Reference data were obtained from the RRUFF database (refs. X050192, X050057.4, and R040059, for enstatite, diopside, and anorthite, respectively).

The characteristic Raman profile of plagioclase feldspars was also observed during the spectroscopic analysis of the QUE (Fig. 8g). The composition of a plagioclase feldspar is typically denoted by its overall fraction of anorthite (An; $\text{CaAl}_2\text{Si}_2\text{O}_8$) or albite (Ab; $\text{NaAlSi}_3\text{O}_8$), the calcium and sodium endmembers of the series, respectively. In the studied sample, the Raman data indicate that the plagioclase material has anorthite as the main component, since the major observed bands,

appearing at 193, 401, 485, 503, 559 and 971 cm^{-1} , are in excellent agreement with the main characteristic bands for this mineral (199, 402, 488, 504, 557 and 984 cm^{-1}) reported by Freeman *et al.* (Freeman *et al.*, 2008) and Mernagh (Mernagh, 1991). The most intense bands at 485 and 503 cm^{-1} have been attributed to mixed Si–O–Si (or Si–O–Al) bending/stretching modes, the 971 cm^{-1} band to non-bridged SiO groups symmetric stretching vibrations, and those within the 450–600 cm^{-1} range to different bending modes of the aluminosilicate network (Furukawa *et al.*, 1981; Mernagh, 1991). It is interesting to note here that the 485 and 503 cm^{-1} bands were also observed for shocked anorthite by Freeman *et al.* at 484.4 and 505.1 cm^{-1} for NWA 773 lunar gabbro (Freeman *et al.*, 2008) exhibiting an $\text{Or}_2\text{Ab}_{10}\text{An}_{88}$ (orthoclase:albite:anorthite) compositional ratio. This composition is also in agreement with the 2013 Cohen's work on the several achondrites, including QUE 97001, where she demonstrated that plagioclase in several 4Vesta originated howardites (eucrites, diogenites) has compositions where anorthite corresponds to wt% 80–95 (Cohen, 2013). The band at 401 cm^{-1} is most probably due to a stretching vibration of the Ca–O moiety, while the lowest frequency band, observed at 193 cm^{-1} , is ascribable to an external lattice mode (chain rotation) (Mernagh, 1991). It is also interesting to note that the spectral profile of the observed plagioclase shows a slight intensity weakening compared to the reference spectrum of anorthite in the spectral region about 1000 cm^{-1} , as well as an increase of the intensity of the band at 485 cm^{-1} compared to the band at 503 cm^{-1} . These observations align with those reported by Velde *et al.*, and Jared *et al.*, who have observed these trends in the Raman spectra of shocked feldspars (in both alkali- or plagioclase-type feldspars) (Velde *et al.*, 1985; Jared *et al.*, 2014; Jared *et al.*, 2018).

Ilmenite (FeTiO_3) was also identified in QUE as seen in Fig. 9a with the reference data (Lafuente *et al.*, 2015) provided in Fig. 9b. Characteristic bands of the mineral are observed at 231, 330, 373 and 683 cm^{-1} in the QUE spectrum, which correspond to those appearing at 226, 330, 367 and 676 cm^{-1} in the spectrum of the reference. Alva-Valdivia and coworkers (Alva-Valdivia *et al.*, 2013) have observed the major band of ilmenite at 220, 398 and 680 cm^{-1} , while Wang *et al.* (Wang *et al.*, 2004) reported bands at 224, 333, 368 and 683 cm^{-1} , assigning the lowest frequency band to a translational lattice mode of the iron atom, the intermediate ones to translational lattice modes of the XO_6 ($\text{X} = \text{Fe}$ or Ti) octahedra, and the more intense higher frequency band to the symmetric stretching vibration of the TiO_6 octahedra. Note that the spectrum in Fig. 9a that the band at 330 cm^{-1} also contains a minor contribution due to enstatite, which also accounts partially for the band observed at 1011 cm^{-1} and to the shoulder at lower frequencies of the band with maximum at 683 cm^{-1} . The band at 393 cm^{-1} , may result from contamination of diopside, which might also contribute to the intensity of the 330, 1010 bands and shoulder in the 660–670 cm^{-1} range.

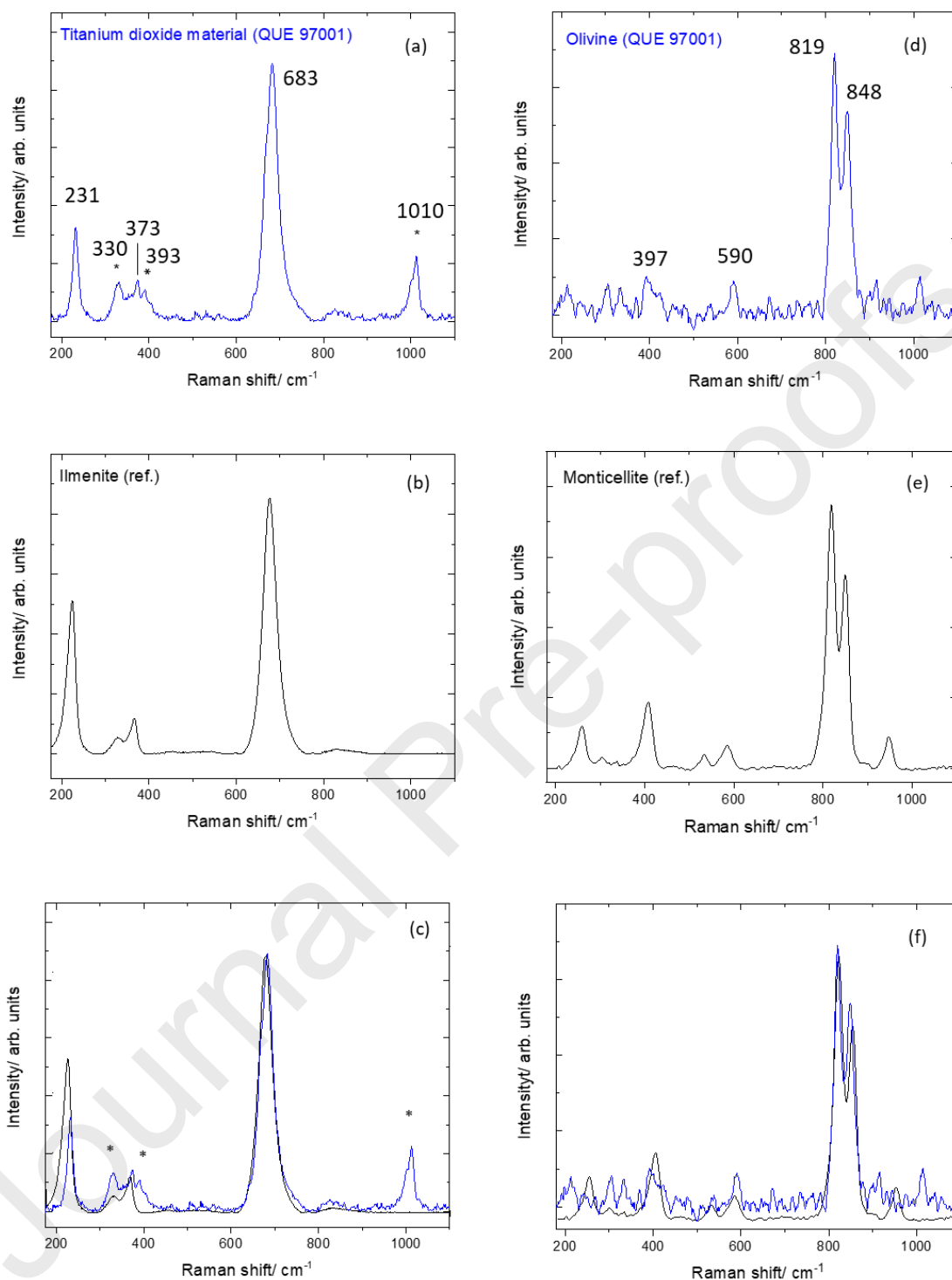


Fig. 9. Raman spectra of the (a) titanium dioxide and (d) olivine group materials obtained from the QUE meteorite sample, and the spectra of the reference minerals, (b) ilmenite and (e) monticellite. The spectra of the observed minerals and of the corresponding references are also plotted together in graphs (c) and (f). Reference data were obtained from the RRUFF database (refs. R130214, and R040115, for ilmenite, and monticellite, respectively). In the meteorite spectrum (a), bands marked with an asterisk and the shoulder about 660-670 cm^{-1} correspond to enstatite/diopside or have substantial contribution from these minerals.

The Raman spectrum of the olivine group material present in the QUE is shown in Fig. 9d. The ratio of magnesium to iron in calcium olivines varies between the two endmembers of the corresponding solid solution series: monticellite (Mg endmember: CaMgSiO_4) and kirschsteinite (Fe endmember: CaFeSiO_4). However, in most of its occurrences this type of mineral has the pure magnesium endmember composition. On the other hand, it is well-known that monticellite (CaMgSiO_4) does not form complete solid solutions with forsterite (Mg_2SiO_4) (Mernagh, 1991), which facilitates the spectroscopic distinction between these two minerals. The comparison of the Raman spectrum of the olivine in QUE with reference data (Chopelas, 1991; Lafuente et al., 2015; Mohanan et al., 1993) demonstrates that with all probability it corresponds to monticellite (Fig. 9e,f). The position of the most intense characteristic bands of olivine, observed in this sample at 819 and 848 cm^{-1} (assigned to Si–O tetrahedral stretching modes), in particular, is a good indicator of the nature of the mineral, as reported in detail by Mohanan and coworkers (Mohanani et al., 1993). In monticellite, the reference values are 818 and 851 cm^{-1} , which match well the observed values for the QUE sample and are considerably distinct from those typical of forsterite (824 and 855 cm^{-1}) (Mohanani et al., 1993). Moreover, monticellite also shows a relatively intense Raman band at 407 cm^{-1} (Ca–O stretching) (Mohanani et al., 1993), which fits well the one observed for QUE at 397 cm^{-1} , while in forsterite the band (Mg–O stretching) appears at a much higher frequency (434 cm^{-1}) (Mohanani et al., 1993). Furthermore, monticellite exhibits a single band at 590 cm^{-1} as observed in the QUE sample, while forsterite shows a doublet of bands at 580 and 605 cm^{-1} (Mohanani et al., 1993). One must however notice the less good agreement between the observed spectrum of the olivine in QUE and the reference spectrum of monticellite in the regions below 300 and above 1000 cm^{-1} , which are spectral regions where the profile of the reference spectra of monticellite is very much sensitive to the experimental conditions (Downs, 2006) and other minerals present in the meteorite do also absorb (see Fig. 8).

Interestingly, the FWHM of the two components of the characteristic olivine doublet of bands are 26 and 17 cm^{-1} , respectively. The measured FWHM values of the two prominent Raman bands of monticellite-type olivine in QUE (26 and 17 cm^{-1}) indicate considerable structural disorder. Compared to unshocked terrestrial olivines, which display narrower bands around 9–10 cm^{-1} (Rull et al., 2010), these broadened bands are indicative of shock metamorphic effects. Based on the correlation between Raman FWHM and shock stage proposed (Rull et al., 2010; Velde et al., 1989), such broadening corresponds to a shock stage of S3 to S4, typically associated with pressures in the range of ~15–35 GPa and post-shock temperatures exceeding 900 °C. These values suggest that the QUE sample experienced significant impact-related deformation, consistent with its brecciated

texture and optical signs of shock metamorphism, such as undulatory extinction and intragranular fracturing observed. (Rull et al., 2010).

These results indicate that a certain structural disorder occurred in the studied samples, which can be caused by the unique conditions and processes that occur in space and during the meteorite's journey to Earth, such as impact- or thermal-induced metamorphism, cosmic rays and solar radiation in space, space weathering, among others. Also, in support with our findings, previous studies on Northwest Africa NWA 7634 (CO3 type meteorite) (“NWA 7634,” 2024) and NWA 8258 (L3 type of meteorite) (“NWA 8258,” 2024) also have found monticellite in these meteorites. It is obvious that there is still a need for more research to further understand the relationship of this particular mineral in different classes of meteorites.

Fig. 10 presents representative 2 mm² Raman maps of the meteorite sample. The colors correspond to the different minerals identified in the sample: red for pyroxenes, green for plagioclase, yellow for ilmenite, and blue for olivine. These maps were generated by using reference spectra for each mineral across the full Raman range (200-1100 cm⁻¹). At this broader scale, the distribution of minerals within the sample appears relatively uniform. As expected based on established data for Howardites of 4Vesta origin, the sample is predominantly composed of pyroxene and plagioclase, with ilmenite occurring in smaller amounts and olivine being the least abundant among the minerals identified by Raman spectroscopy.

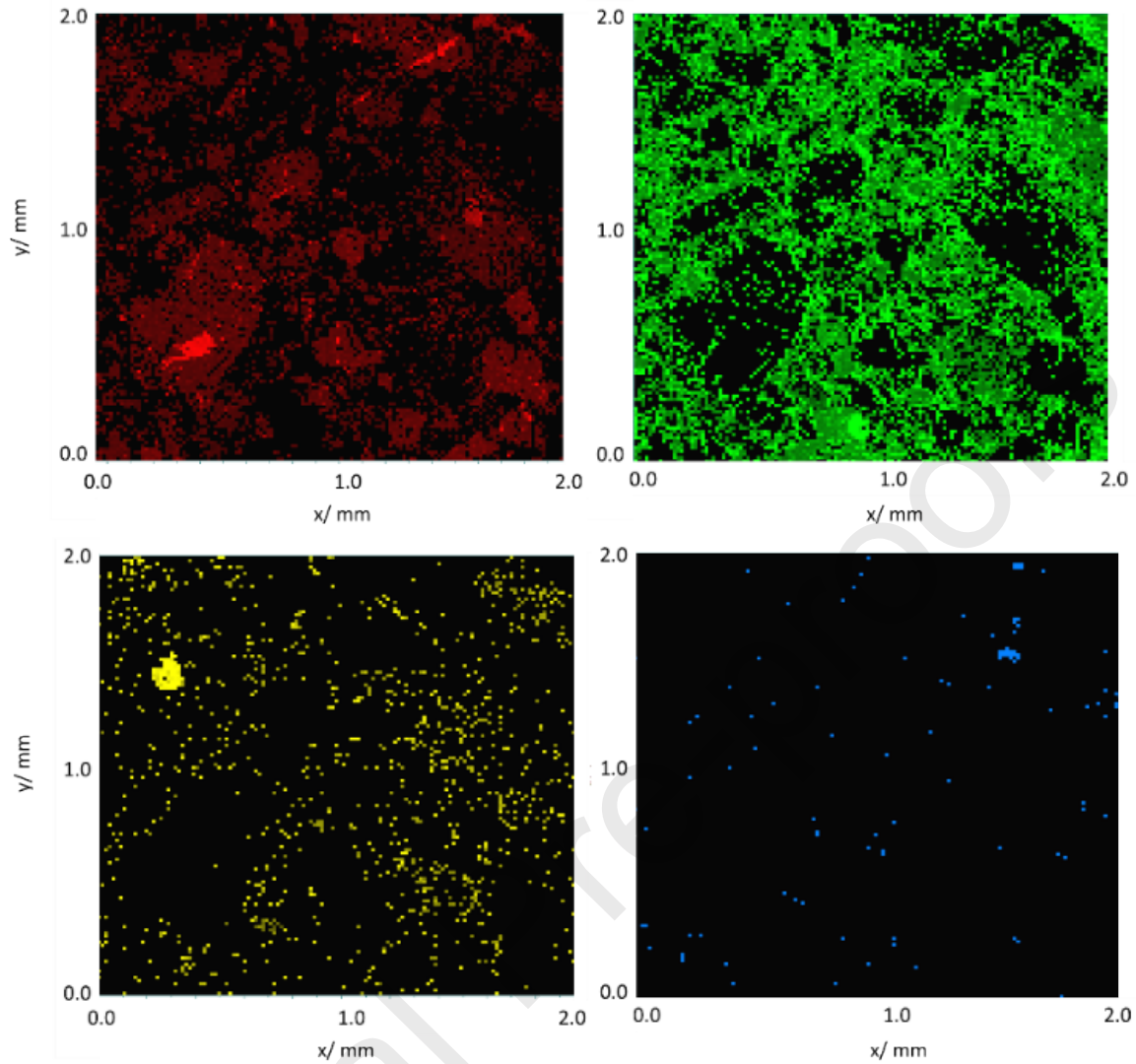


Fig. 10. Raman maps showing mineralogical distribution in QUE. (Red: px, green: pl; yellow: il; blue: ol).

3.4.2. EET sample

In the EET sample, the collected Raman spectra allowed identification of two different minerals from the orthopyroxene series, one with major percentage of enstatite ($\text{En}_{80}\text{Fs}_{20}$) and the second with an increased percentage of ferrosilite (between 40 and 50% Fs), the clinopyroxene diopside, the plagioclase feldspar anorthite, and the olivine forsterite. The spectra of the minerals identified in both the EET and QUE Raman spectra do not differ substantially. Fig. 11 presents the spectra of the EET ferrosilite-rich orthopyroxene phase, and that of ferrosilite, and that of the olivine minerals found in the two meteorite samples together with reference spectra of forsterite and monticellite (Lafuente et al., 2015; Downs, 2006).

The spectrum of the ferrosilite-rich orthopyroxene phase of EET shows bands at 330 (Mg/Fe–O stretching), 387 (SiO bending), 656/673 (Si–O–Si bridging symmetric stretching), and 1002 (non-bridging SiO symmetric stretching) cm^{-1} , at similar but distinct frequencies observed in both the enstatite-rich orthopyroxene phase of EET and the orthopyroxene mineral found in the QUE (see above), and matching well the expected frequency ranges for a orthopyroxene material with a composition with a percentage of ferrosilite between 40 and 50%: 327-321, 383-390, 652-655, 671-675, 1003-1004 cm^{-1} , respectively (Huang et al., 2000). This finding of Fs% ~50 from the pyroxene bands in our study is in line with the Burbine et al.'s work, where it was shown that EET has an $\text{En}_{52}\text{Fs}_{40}\text{Wo}_8$ pyroxene composition (Burbine et al., 2001).

In relation to the identified olivine, the intense SiO tetrahedral stretching mark-bands were observed at 824 and 855 cm^{-1} , matching the reference values for forsterite (Fig. 11c,d) (Mohan et al., 1993). In Fig. 11, the spectra of the olivine phase of the QUE sample, identified as monticellite (see above), and the reference spectrum of this mineral are also presented to highlight the differences between the two olivine-type materials.

Characteristic 1 mm^2 Raman maps of the meteorite sample, made using the spectrum of each mineral as reference in the full spectroscopic range (200-1100 cm^{-1}), are shown in Fig. 12, the colors used to build the maps corresponding to the different types of minerals identified by Raman spectroscopy: red, pyroxenes; green, plagioclase; blue, olivine. As for the QUE, at this broader scale, the distribution of minerals within the sample appears relatively uniform and, also as expected based on established data for Howardites of 4Vesta origin, the sample is predominantly composed of pyroxenes and plagioclase, with olivine (forsterite in this case) being the least abundant among the minerals identified by Raman spectroscopy.

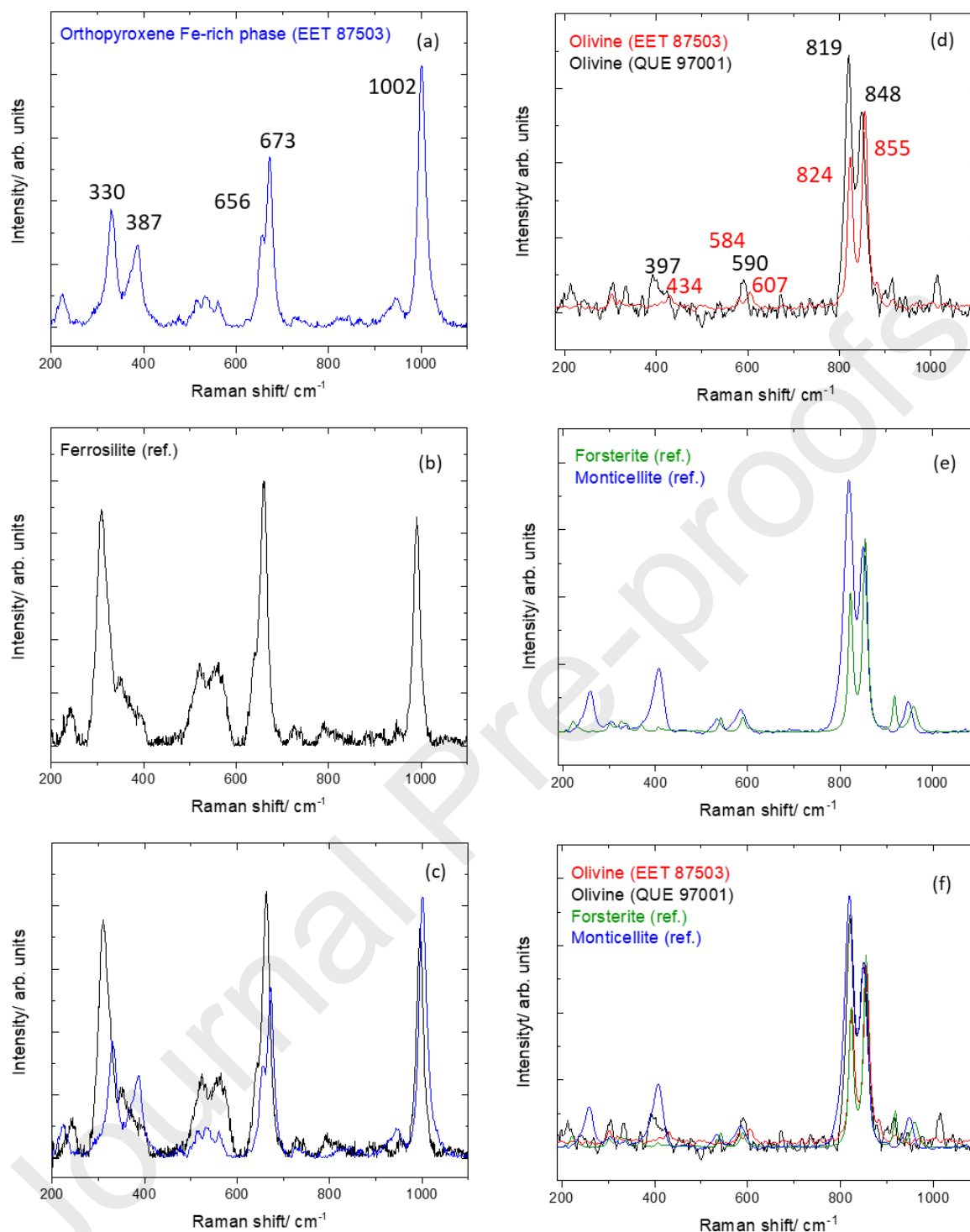


Fig. 11. Raman spectra of the (a) Fs-rich orthopyroxene phase of EET meteorite sample and (d) olivine group materials obtained from the EET and QUE meteorite samples, and the spectra of the corresponding reference minerals, (b) ferrosilite and (e) forsterite and monticellite. The spectra of the observed minerals and of the corresponding references are also plotted together in graphs (c) and (f). Reference data were obtained from the RRUFF database (refs. R070386, X050087, and R040115, forsterite, and monticellite, respectively).

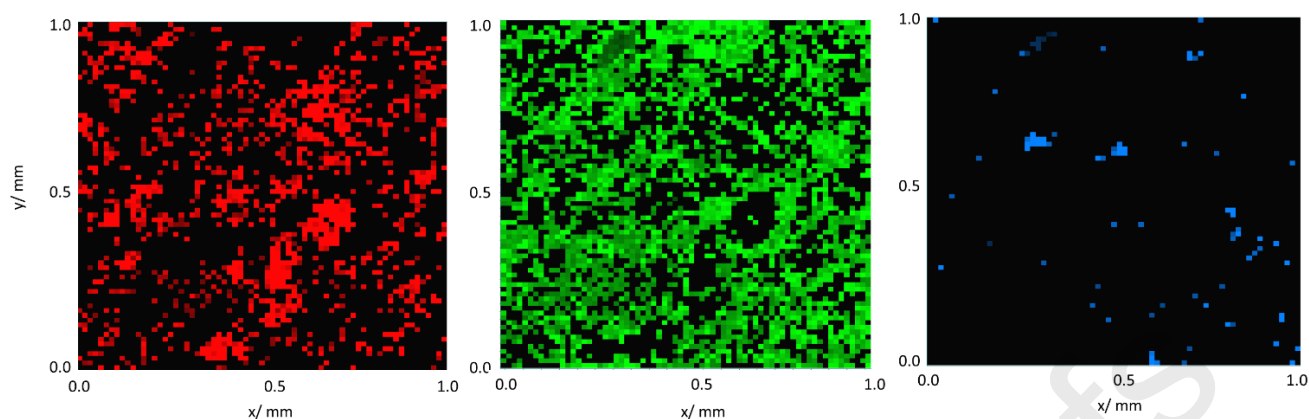


Fig. 12. Raman maps showing the minerals distribution in the EET. Color codes: red, pyroxenes; green, plagioclase; blue, olivine.

As a whole, the Raman results agree very well with the optical microscopy analysis for both meteorite samples, allowing the identification of the specific materials that were also observed by microscopy, in particular in the case of the microscopy observed plagioclases, which were shown to be predominantly anorthite, and olivines, which were identified by Raman as being mostly monticellite in QUE and forsterite in EET, but also in the case of the clinopyroxene-type material, identified by Raman as being diopside. The orthopyroxene enstatite was shown to be dominant in both meteoritic samples, with a Fs-rich phase also identified in EET. Ilmenite was also determined to be present in the QUE sample by Raman spectroscopy, while both the chrome bearing mineral observed by optical microscopy and troilite were not detected by Raman, due to their low abundance in the samples.

These results, including undulatory extinction, intragranular fracturing, and broadened Raman bands (FWHM of 26–17 cm^{-1} in olivine), indicate that the samples experienced moderate to high shock stages (S3–S4). The associated pressure-temperature regime (15–35 GPa, >900 °C) is consistent with impact processing within the upper crust of a differentiated planetary body, such as 4 Vesta, suggesting a complex collisional history and partial thermal annealing of mineral phases.

The extent of terrestrial weathering in both QUE and EET samples appears to be minimal, as inferred from TGA and optical microscopy results. The TGA data revealed no significant mass loss below 200 °C, a temperature range typically associated with the release of adsorbed water and loosely bound hydroxyls in weathered meteorites. This absence of low-temperature devolatilization peaks suggests minimal hydration or clay formation. Furthermore, the petrographic observations show clean grain boundaries without clay rims, oxidation halos, or pervasive fracturing—all features commonly associated with weathering. These indicators collectively point to a low weathering rate, consistent

with Antarctic preservation environments and suggest a weathering grade between A and B according to the standard Antarctic meteorite weathering scale.

4. Conclusion

In this study, the Antarctic howardite meteorites EET 87503 and QUE 97001 were investigated by a combined approach that joins optical microscopy, Raman spectroscopy, and calorimetric techniques (DSC and TGA). DSC experiments focused on the troilite α/β phase transition investigation, which was found to take place in the EET and QUE studied samples at 146.66 and 147.50 °C, respectively, indicating a 0.26% and 0.13% troilite content in the meteorites, respectively. TGA indicated minor weight loss (< 1%) in both samples upon heating the samples up to 1200 °C. The optical microscopy and Raman spectroscopy analysis agreed in relation to the presence in the meteorites of plagioclase minerals, which were shown to be predominantly anorthite, olivines, which very interestingly were identified by Raman as being mostly monticellite in QUE and forsterite in EET, the clinopyroxene diopside, and the orthopyroxene enstatite, which was shown to be dominant in both meteoritic samples, with a ferrosilite-rich phase also identified in EET. Ilmenite was also determined to be present in the QUE sample by Raman spectroscopy, while both the chrome bearing mineral observed by optical microscopy and troilite were not detected by Raman, due to their low abundance in the samples. The richness of minerals found in the meteorites and their characteristics suggest the complex thermal and impact histories of the studied howardites. As a whole, the results obtained in the present study are a contribution to a better understanding of the mineralogy and thermal evolution of this type of meteorites, linking them to potential parent bodies such as asteroid 4Vesta.

At this point, we have to emphasize and admit that while our combined use of optical microscopy and Raman spectroscopy has allowed for detailed mineralogical characterization of the howardite samples EET 87503 and QUE 97001, the absence of in situ quantitative compositional data from electron microprobe analysis (EMPA) imposes certain analytical limitations. Optical microscopy, even when coupled with polarized light techniques, offers only qualitative to semi-quantitative insights into mineral textures, optical properties, and shock features, but it cannot resolve subtle compositional heterogeneities or solid solution series variations—particularly within the pyroxene (e.g., enstatite–ferrosilite–hedenbergite) and plagioclase (e.g., anorthite–albite–orthoclase) groups. While Raman spectroscopy enhances phase identification and allows indirect inference of mineral composition based on band positions and FWHM values, this approach is inherently constrained by overlapping bands, orientation effects, and the lack of absolute elemental quantification. The inability to obtain precise Mg/Fe or Ca/Na ratios, zoning patterns, or trace element data may lead to

overgeneralizations in phase assignment (e.g., distinguishing intermediate compositions or identifying exsolution textures). Furthermore, without EMPA confirmation, the estimation of shock stage from birefringence behavior or Raman band broadening remains interpretative rather than definitive. These limitations should be considered when evaluating our conclusions regarding the samples' thermal metamorphic conditions, impact histories, and potential derivation from heterogeneous crustal domains of 4 Vesta. Future work incorporating high-resolution quantitative microanalytical techniques (e.g., EMPA, SEM-EDS, or LA-ICP-MS) would greatly enhance the robustness of the mineralogical interpretations and deepen our understanding of HED brecciation and regolith evolution.

Acknowledgements

This work was supported by the National Aeronautics and Space Administration (NASA) Johnson Space Center (JSC). O.U and C.A.U. are grateful for the support of this project by Ege University Scientific Research Projects Coordination Unit with Project Number 17-FEN-050. B.A.N. and R. F. acknowledge financial support from the Portuguese Science Foundation (“Fundação para a Ciência e a Tecnologia” - FCT) – Projects CQC UIDB/00313/2020 and UIDP/00313/2020. Access to instruments from Laser-Lab Coimbra, funded under QREN-Mais Centro, is gratefully acknowledged. B.A.N. also acknowledges FCT for the SFRH/BD/129852/2017 PhD Scholarship. “US Antarctic meteorite samples are recovered by the Antarctic Search for Meteorites (ANSMET) program which has been funded by NSF and NASA and characterized and curated by the Department of Mineral Sciences of the Smithsonian Institution and Astromaterials Acquisition and Curation Office at NASA Johnson Space Center”. The Horizon-Widerra-2023-Talents-01 ERA-Chair 1011848998 Spectroscopy@IKU “Manipulating and Characterizing Molecular Architectures: From Isolated Molecules to Molecular Crystals” is Funded by the European Union.

References

- Allton, J.H., Wentworth, S.J., Gooding, J.L., 1994. Calorimetric thermometry of meteoritic troilite: Preliminary thermometer relationships, in: *The Twenty-Fifth Lunar and Planetary Science Conference*. pp. 25–26.
- Alton, J.H., S.J., W., J.L., G., 1994. Calorimetric thermometry of meteoritic troilite; preliminary thermometer relationships, in: *Lunar and Planetary Science Conference, XXV*. pp. 25–26.
- Altunayar-Unsalan, C., Unsalan, O., 2022. The determination of the water content and hydrogen abundance of two CK- and CV-type carbonaceous chondrites using thermogravimetric analysis. *Int. J. Thermophys.* 43, 1–11. <https://doi.org/10.1007/s10765-022-03064-3>
- Altunayar-Unsalan, C., Unsalan, O., Szurgot, M.A., Wach, R.A., 2021. Specific heat and thermal history of the Sariçiçek howardite. *Meteorit. Planet. Sci.* 56, 2103–2117. <https://doi.org/10.1111/maps.13754>
- Altunayar-Unsalan, C., Unsalan, O., Wach, R., Szurgot, M.A., 2025. Physical and thermal properties of Bursa L6 chondrite : a combination of density , porosity , specific heat , water content , thermal conductivity , and thermal diffusivity results. *Astrophys Sp. Sci* 370, 1–21. <https://doi.org/10.1007/s10509-025-04443-6>
- Alva-Valdivia, L.M., Rivas-Sánchez, M. de la L., Arenas-Alatorre, J., Goguitchaishvili, A., Lopes, O.F., 2013. Microscopy and rock magnetism of fine grain-size titanomagnetite from the Jacupiranga Alkaline Complex, Brazil: Unearthing Ti-magnesioferrite nanoparticles. *Geofis. Int.* 52, 93–110. [https://doi.org/10.1016/s0016-7169\(13\)71465-x](https://doi.org/10.1016/s0016-7169(13)71465-x)
- Burbine, T.H., Buchanan, P.C., Binzel, R.P., Bus, S.J., Hiroi, T., Hinrichs, J.L., Meibom, A., McCoy, T.J., 2001. Vesta, Vestoids, and the howardite, eucrite, diogenite group: Relationships and the origin of spectral differences. *Meteorit. Planet. Sci.* 36, 761–781. <https://doi.org/10.1111/j.1945-5100.2001.tb01915.x>
- Chopelas, A., 1991. Single crystal Raman spectra of forsterite, fayalite, and monticellite. *Am. Mineral.* 76, 1101–1109.
- Cohen, B.A., 2013. The Vestan cataclysm: Impact-melt clasts in howardites and the bombardment history of 4 Vesta. *Meteorit. Planet. Sci.* 48, 771–785. <https://doi.org/10.1111/maps.12101>
- Downs, R.T., 2006. The RRUFF Project: An Integrated Study of the Chemistry, Crystallography, Raman and Infrared Spectroscopy of Minerals, in: *Proceedings of the 19th General Meeting of the International Mineralogical Association*. Scientific Research, Kobe, pp. 3–13.
- Duke, M.B., Silver, L.T., 1967. Petrology of eucrites, howardites and mesosiderites. *Geochim. Cosmochim. Acta* 31, 1637–1665. [https://doi.org/https://doi.org/10.1016/0016-7037\(67\)90112-3](https://doi.org/https://doi.org/10.1016/0016-7037(67)90112-3)

- Etchepare, J., 1972. Study by Raman spectroscopy of crystalline and glassy diopside, in: Douglas, R.W., Ellis, B. (Eds.), *Morphous Materials International Conference on Noncrystalline Solids*. Wiley Interscience, London, pp. 337–346.
- Freeman, J.J., Wang, A., Kuebler, K.E., Jolliff, B.L., Haskin, L.A., 2008. Characterization of natural feldspars by raman spectroscopy for future planetary exploration. *Can. Mineral.* 46, 1477–1500. <https://doi.org/10.3749/canmin.46.6.1477>
- Furukawa, T., Fox, K.E., White, W.B., 1981. Raman spectroscopic investigation of the structure of silicate glasses. III. Raman intensities and structural units in sodium silicate glasses. *J. Chem. Phys.* 75, 3226–3237. <https://doi.org/10.1063/1.442472>
- Garenne, A., Beck, P., Montes-Hernandez, G., Chiriac, R., Toche, F., Quirico, E., Bonal, L., Schmitt, B., 2014. The abundance and stability of “water” in type 1 and 2 carbonaceous chondrites (CI, CM and CR). *Geochim. Cosmochim. Acta* 137, 93–112. <https://doi.org/10.1016/j.gca.2014.03.034>
- Hodges, Z.V., Mittlefehldt, D.W., 2017. Petrology of igneous clasts in regolithic howardite EET 87503, in: *Lunar and Planetary Science XLVIII*. pp. 1339–1340.
- Huang, E., Chen, C.H., Huang, T., Lin, E.H., Xu, J.A., 2000. Raman spectroscopic characteristics of Mg-Fe-Ca pyroxenes. *Am. Mineral.* 85, 473–479. <https://doi.org/10.2138/am-2000-0408>
- Jaret, S.J., Kah, L.C., Harris, R.S., 2014. Progressive deformation of feldspar recording low-barometry impact processes, Tenoumer impact structure, Mauritania. *Meteorit. Planet. Sci.* 49, 1007–1022. <https://doi.org/10.1111/maps.12310>
- Kakkala, M., 1993. *Vibrational spectroscopic studies of olivines, pyroxenes, and amphiboles at high temperatures and pressures*. University of Hawaii.
- King, A.J., Solomon, J.R., Schofield, P.F., Russell, S.S., 2015. Characterising the CI and CI-like carbonaceous chondrites using thermogravimetric analysis and infrared spectroscopy. *Earth, Planets Sp.* 67, 198. <https://doi.org/10.1186/s40623-015-0370-4>
- Lafuente, B., Downs, R.T., Yang, H., Stone, N., 2015. The power of databases: the RRUFF project, in: Armbruster, T., Danisi, R.M. (Eds.), *Highlights in Mineralogical Crystallography*. W. De Gruyter, pp. 1–30.
- List of howardites in Meteoritical Bulletin, 2024. . *Meteorit. Bull. Database*.
- Maksimova, A.A., Unsalan, O., Chukin, A.V., Karabanalov, M.S., Jenniskens, P., Felner, I., Semionkin, V.A., Oshtrakh, M.I., 2020. The interior and the fusion crust in Sariçiçek howardite: Study using X-ray diffraction, magnetization measurements and Mössbauer spectroscopy. *Spectrochim. Acta - Part A Mol. Biomol. Spectrosc.* 228. <https://doi.org/10.1016/j.saa.2019.117819>

- Maksimova, A.A., Unsalan, O., Chukin, A. V., Oshtrakh, M.I., 2019. Comparison of the 57 Fe hyperfine interactions in silicate phases in Sariçiçek howardite and some ordinary chondrites. *Hyperfine Interact.* 240. <https://doi.org/10.1007/s10751-019-1593-8>
- Mayne, R.G., Smith, S.E., Corrigan, C.M., 2016. Hiding in the howardites: Unequilibrated eucrite clasts as a guide to the formation of Vesta's crust. *Meteorit. Planet. Sci.* 51, 2387–2402. <https://doi.org/10.1111/maps.12730>
- Mernagh, T.P., 1991. Use of the laser Raman microprobe for discrimination amongst feldspar minerals. *J. Raman Spectrosc.* 22, 453–457. <https://doi.org/10.1002/jrs.1250220806>
- Meteoritical Bulletin Database, 2025. . Meteorit. Bull. Database.
- Mittlefehldt, D.W., Herrin, J.S., Quinn, J.E., Mertzman, S.A., Cartwright, J.A., Mertzman, K.R., Peng, Z.X., 2013. Composition and petrology of HED polymict breccias: The regolith of (4) Vesta. *Meteorit. Planet. Sci.* 48, 2105–2134. <https://doi.org/10.1111/maps.12182>
- Miyamoto, M., Takeda, H., Yanai, K., 1978. Yamato achondrite polymict breccias, in: *Memoirs of National Institute of Polar Research, Special Issue, Proceedings of the Second Symposium on Yamato Meteorites.* pp. 185–197.
- Mohanan, K., Sharma, S.K., Bishop, E.C., 1993. A Raman spectral study of forsterite-monticellite solid solutions. *Am. Mineral.* 78, 42–48.
- Moskovitz, N.A., Willman, M., Burbine, T.H., Binzel, R.P., Bus, S.J., 2010. A spectroscopic comparison of HED meteorites and V-type asteroids in the inner Main Belt. *Icarus* 208, 773–788. <https://doi.org/10.1016/j.icarus.2010.03.002>
- Nakashima, D., Kita, N.T., Ushikubo, T., Noguchi, T., Nakamura, T., Valley, J.W., 2013. Oxygen three-isotope ratios of silicate particles returned from asteroid Itokawa by the Hayabusa spacecraft: A strong link with equilibrated LL chondrites. *Earth Planet. Sci. Lett.* 379, 127–136. <https://doi.org/10.1016/j.epsl.2013.08.009>
- NWA 7634, 2024. . Meteorit. Bull. Database.
- NWA 8258, 2024. . Meteorit. Bull. Database.
- Potin, S., Beck, P., Bonal, L., Schmitt, B., Garenne, A., Moynier, F., Agranier, A., Schmitt-Kopplin, P., Malik, A.K., Quirico, E., 2020. Mineralogy, chemistry, and composition of organic compounds in the fresh carbonaceous chondrite Mukundpura: CM1 or CM2? *Meteorit. Planet. Sci.* 55, 1681–1696. <https://doi.org/10.1111/maps.13540>
- Prencipe, M., Mantovani, L., Tribaudino, M., Bersani, D., Lottici, P.P., 2012. The Raman spectrum of diopside: a comparison between ab initio calculated and experimentally measured frequencies. *Eur. J. Mineral.* 24, 457–464. <https://doi.org/10.1127/0935-1221/2012/0024-2178>
- Richter, K., 2020. Vesta and Ceres. <https://doi.org/10.1093/acrefore/9780190647926.013.34>

- Rull, F., Muñoz-Espadas, M.J., Lunar, R., Martínez-Frías, J., 2010. Raman spectroscopic study of four Spanish shocked ordinary chondrites: Cañellas, Olmedilla de Alarcón, Reliegos and Olivenza. *Philos. Trans. R. Soc. A Math. Phys. Eng. Sci.* 368, 3153–3166.
<https://doi.org/10.1098/rsta.2010.0104>
- Stöffler, K., Keil, K., Scott, E.R.D., 1991. <Shock metamorphism of ordinary chondrites.pdf>. *Geochim. Cosmochim. Acta* 55, 3845–3867.
- Szurgot Wach, Radoslaw A., Przylibski, T., M., 2012. Thermophysical properties of the Sołtmany Meteorite. *Meteorites* 2, 53–65. <https://doi.org/10.5277/met120107>
- Szurgot Wach, Radoslaw A., Przylibski, T., M., 2012. Thermophysical properties of the Sołtmany Meteorite. *Meteorites* 2, 53–65. <https://doi.org/10.5277/met120107>
- Tian, Z., 2021. Potassium isotope cosmochemistry. Washington University in St. Louis.
- Unsalan, O., Jenniskens, P., Yin, Q.Z., Kaygisiz, E., Albers, J., Clark, D.L., Granvik, M., Demirkol, I., Erdogan, I.Y., Bengu, A.S., Özel, M.E., Terzioglu, Z., Gi, N., Brown, P., Yalcinkaya, E., Temel, T., Prabhu, D.K., Robertson, D.K., Boslough, M., Ostrowski, D.R., Kimberley, J., Er, S., Rowland, D.J., Bryson, K.L., Altunayar-Unsalan, C., Rangelov, B., Karamanov, A., Tatchev, D., Kocahan, Ö., Oshtrakh, M.I., Maksimova, A.A., Karabanalov, M.S., Verosub, K.L., Levin, E., Uysal, I., Hoffmann, V., Hiroi, T., Reddy, V., Ildiz, G.O., Bolukbasi, O., Zolensky, M.E., Hochleitner, R., Kaliwoda, M., Öngen, S., Fausto, R., Nogueira, B.A., Chukin, A. V., Karashanova, D., Semionkin, V.A., Yeşiltaş, M., Glotch, T., Yilmaz, A., Friedrich, J.M., Sanborn, M.E., Huyskens, M., Ziegler, K., Williams, C.D., Schönbacher, M., Bauer, K., Meier, M.M.M., Maden, C., Busemann, H., Welten, K.C., Caffee, M.W., Laubenstein, M., Zhou, Q., Li, Q.L., Li, X.H., Liu, Y., Tang, G.Q., Sears, D.W.G., Mclain, H.L., Dworkin, J.P., Elsilá, J.E., Glavin, D.P., Schmitt-Kopplin, P., Ruf, A., LE Corre, L., Schmedemann, N., 2019. The Sariçiçek howardite fall in Turkey: Source crater of HED meteorites on Vesta and impact risk of Vestoids. *Meteorit. Planet. Sci.* 54, 953–1008. <https://doi.org/10.1111/maps.13258>
- Velde, B., Syono, Y., Kikuchi, M., Boyer, H., 1989. Raman microprobe study of synthetic diaplectic plagioclase feldspars. *Phys. Chem. Miner.* 16, 436–441. <https://doi.org/10.1007/BF00197013>
- Wahl, W., 1952. The brecciated stony meteorites and meteorites containing foreign fragments. *Geochim. Cosmochim. Acta* 2, 91–117.
- Wang, A., Kuebler, K.E., Jolliff, B.L., Haskin, L.A., 2004. Raman spectroscopy of Fe-Ti-Cr-oxides, case study: Martian meteorite EETA79001. *Am. Mineral.* 89, 665–680.
<https://doi.org/10.2138/am-2004-5-601>

Highlights

- Antarctic howardites, EET 87503 and QUE 97001, were investigated by Raman spectroscopy, optical microscopy, DSC, and TGA.
- A rare magnesium-end-member silicate, monticellite, was identified in both meteorites, offering insights into the thermal and impact histories of these howardites.
- Troilite contents of 0.26 and 0.13% for EET and QUE, respectively indicate variations in their thermal histories.
- TGA showed minimal weight loss (<1%) upon heating to 1200°C, suggesting that both meteorites are largely stable

The authors declare that they have no known competing financial interests or personal relationships that could have appeared to influence the work reported in this paper.